Applied Catalysis B: Environmental 327 (2023) 122440

Contents lists available at ScienceDirect

Applied Catalysis B: Environmental

journal homepage: www.elsevier.com/locate/apcatb

Long-lasting performance of high-flux perovskite membrane for catalytic degradation of organic pollutants

Jinping Liang [a,b,c,*], Kai Gao [a], Aijuan Zhou [a], Yuqiao Fang [a], Shengyou Su [a], Ling Fu [a], Mingchao Sun [a], Xiaoguang Duan [d,**]

[a] College of Chemistry and Materials Science, Sichuan Normal University, Chengdu 610066, China
[b] Sichuan Engineering Laboratory of Livestock Manure Treatment and Recycling, Chengdu 610066, China
[c] Key Laboratory of Treatment for Special Wastewater of Sichuan Province Higher Education System, Chengdu 610066, China
[d] School of Chemical Engineering, The University of Adelaide, Adelaide SA5005, Australia

ARTICLE INFO

Keywords:
Cobalt-based perovskite
Peroxymonosulfate
High-flux membrane
Radical oxidation
Long-term stability

ABSTRACT

Membrane separation for wastewater remediation has been perplexed by membrane fouling, and the design of highly antifouling membranes for high-flux operation remains challenging. Herein, $Sm_{0.5}Sr_{0.5}CoO_{3-\delta}$ (SSC700) membrane was coupled with peroxymonosulfate (PMS) catalysis. SSC700 demonstrated superb efficacy in batch and fixed-bed reactions, generating sulfate radicals ($SO_4^{-\bullet}$) and hydroxyl radicals (HO•) for pollutants oxidation. Additionally, in robust SSC700 membrane/PMS systems, Rhodamine B (RhB) realized > 91% removal for 50 h from laboratory wastewater under fluxes above 368 L/(m^2·h), and strikingly, ciprofloxacin, RhB and sulfamerazine in the secondary effluent attained 60–80% (50 h), almost 100% (100 h) and 50–60% (50 h) removal under fluxes around 1000, 600 and 900 L/(m^2·h), respectively. The highly reactive $Co^{2+}/Co^{3+}/Co^{4+}$ redox couples accounted for the prominent activity, stability and antifouling capability of SSC700 membranes. Apart from Co species, Sm/Sr played significant roles in organics degradation. Also, bio-toxicity evolution during ciprofloxacin mineralization was monitored. This study dedicates to the design of functional membranes/PMS integrated systems for synergistic wastewater decontamination and membrane defouling.

1. Introduction

Persulfate-based advanced oxidation processes (PS-AOPs) have been promoted as alternatives to Fenton/Fenton-like processes for removing recalcitrant pollutants from wastewater by leveraging sulfate radicals ($SO_4^{-\bullet}$) [1]. Compared with hydroxyl radicals (HO•) in Fenton/Fenton-like processes, $SO_4^{-\bullet}$ has merits of higher oxidation capability (2.5 –3.1 V vs 1.8 –2.8 V), a longer lifespan (30 –40 μs vs ~1 μs of HO•), higher flexibility in terms of pH (3 –9 vs 2 –4 of Fenton reaction) and selectivity, rendering PS-AOPs promising technologies for industrial application [2]. Particularly, catalytic activation of peroxymonosulfate (PMS) is easier than peroxydisulfate (PDS) because of asymmetric structure ($HO-O-SO_3^-$) and longer superoxide O–O bond (1.326 Å vs 1.322 Å) [3]. Therefore, PMS-mediated remediation of refractory organic contaminants has drawn growing attention in the fields.

PMS can be activated by a diversity of strategies, including thermolysis [4], photolysis [2], and chemical reduction [5]. Heterogeneous catalysts, such as metals/oxides [6] and carbonaceous materials [7], have the advantages of low energy input and convenient catalysts recovery. However, metals/oxides suffer from metal ions leaching, while carbonaceous materials are generally subjected to insufficient kinetics in long-term operations due to surface oxidation [8]. Recently, perovskite-type metal oxides (ABO_3) have demonstrated superior activity for generating reactive oxidative species (ROS) from PMS due to their flexible structure and redox property, chemical and thermal stability and low costs [9,10]. B-site elements consist of transitional metals, such as Co, Fe, Mn or Cu, which are typically the active sites in catalysis. A-site elements are alkali/alkaline/rare earth metals, functioning as ideal adsorption sites for target molecules. More importantly, the catalytic performance of perovskites can be precisely regulated by partial substitution of A- or B-site cations. For instance, during PMS-mediated metronidazole (MNZ) degradation, the turnover frequency (TOF) value improved from 7.9 to 12.6 min^{-1}, and simultaneously, cobalt leaching concentration reduced from 1.71 to 0.20 mg/L through Ca and

* Corresponding author at: College of Chemistry and Materials Science, Sichuan Normal University, Chengdu 610066, China.
** Corresponding author.
E-mail addresses: jinpingliang@163.com (J. Liang), xiaoguang.duan@adelaide.edu.au (X. Duan).

https://doi.org/10.1016/j.apcatb.2023.122440
Received 21 October 2022; Received in revised form 14 January 2023; Accepted 7 February 2023
Available online 11 February 2023

Ti doping in A- and B-site of $LaCoO_3$, respectively [11]. Also, appropriate modification can lead to the formation of surface defects and variable oxidation states of B-site elements. For example, the plentiful Co^{2+} sites, surface —OH and oxygen vacancies profited from B-site deficiency in $LaCoO_{3-\delta}$ was revealed to promote catalytic activity, whereas A-site deficiency was pernicious to PMS activation [12]. Therefore, perovskite catalysts with high activity and stability in persulfate chemistry are of industrial demands, thanks to the feasibility and diversity of elaborate composition design and property modulation.

More significantly from an industrial perspective, catalysts recycling and reactivation are indispensable to the currently prevailing batch processes. The arduous labor increases operational costs in industrial applications. Furthermore, some catalysts are practically difficult to be separated from the solution, especially nanoparticles and ultrafine powders. Thus, it is imperative to pursue catalysts with high activity and stability for PMS activation in continuous and long-term operation, e.g., the encouraging membrane separation technology, which is well known for high efficiency, facile operation and low cost but facing a grand challenge of antifouling membrane design [13,14].

One reliable solution to the above problems is developing catalytic membranes by coupling with PS-AOPs, in which the in-situ generated ROS may be devoted to both organics removal and membrane defouling [15]. Additionally, in view of ROS utilization efficiency, a large quantity of ROS are not able to participate in batch operations because of the fulminant generation at the dosing moment and the immediate self-quenching or quenching by solvent. By contrast, this could be effectively avoided in a continuous-flow system, resulting in much higher ROS utilization efficiency. As a proof-of-concept, Bao et al. [16] prepared a pore-functionalized ceramic membrane impregnated with cobalt oxide (CoCM) for PMS-mediated degradation of sulfamethoxazole (SMX), and CoCM exhibited superior antifouling property and decent pure water permeability. Li's group also fabricated a CuO-doped ceramic hollow fiber membrane and systematically investigated its performance in the combined peroxymonosulfate/membrane filtration system for Rhodamine B (RhB) degradation [17]. The system demonstrated a pure water flux of 1255 L/(m^2·h·bar) with high RhB removal efficiency (81.5% within 60 min). These findings evidenced the prominence of PS-AOPs/membrane coupling systems. However, on the one hand, the operating cycles are limited in these works, and few reports emphasized the performance of catalytic membrane/PS-AOPs coupling systems under long-lasting and high-flux operations. On the other hand, ceramics have merely behaved as supports to anchor metal oxides to inhibit heavy metal leaching in previous studies. Since the PMS-active perovskites are ceramics of high-quality in many fields such as energy transfer, we hypothesize that perovskite ceramics may be the chosen one as both the separation membrane and the catalyst for membrane/PMS integrated systems toward wastewater decontamination. Yet, the feasibility and efficacy of these unique systems for refractory organics remediation and membrane defouling under long-lasting and high-flux operations remains unknown.

Herein, we prepared $Sm_{0.5}Sr_{0.5}CoO_{3-\delta}$ (SSC) catalysts by a facile combustion route and investigated their performances for PMS activation and organics degradation. SSC membrane/PMS coupling systems were constructed. This work primarily aims to elucidate the underlying PMS activation mechanisms and to evaluate the long-term stability of SSC membranes for contaminants removal and membrane defouling under high-flux operations, especially in treating secondary effluents. Also, the mineralization pathways and the toxicity of the intermediates were carefully analyzed.

2. Experimental section

2.1. Chemicals and reagents

$Sm(NO_3)_3$·6 H_2O, $Sr(NO_3)_2$, $Co(NO_3)_2$·6 H_2O and glycine were obtained from Chengdu Kelong Chemical Co., Ltd. (P.R.China). Ciprofloxacin (CIP), potassium monopersulfate triple salt ($KHSO_5$·0.5 $KHSO_4$·0.5 K_2SO_4, PMS) and sulfamerazine (SMR) were purchased from Aladdin Industrial Corporation. Other chemicals and reagents were given in Text S1. All chemicals were used as received without any further purification.

2.2. Synthesis of SSC catalysts

$Sm_{0.5}Sr_{0.5}CoO_{3-\delta}$ (SSC) catalysts were synthesized through glycine-assisted solution combustion according to a previous report [18]. Specifically, $Sm(NO_3)_3$·6 H_2O (5 mmol), $Sr(NO_3)_2$ (5 mmol) and Co $(NO_3)_2$·6 H_2O (10 mmol) were dissolved into deionized (DI) water (100 mL) to form homogeneous solution, followed by the addition of glycine (60 mmol). After 30 min vigorous stirring, the solution was concentrated by heating in an evaporating dish until the precursor salts precipitated. Subsequently, the powder mixture was collected and calcined in a muffle furnace at different temperatures from 600 to 900 ºC for 5 h with a ramping rate of 5 °C/min, denoted as SSC600, SSC700, SSC800 and SSC900, respectively.

To evaluate the influences of A-site elements, catalysts with different Sm/Sr ratios (1.0/0, 0.7/0.3, 0.3/0.7 and 0/1.0) were also prepared in the same way as the above, denoted as SmC, SSC73, SSC37 and SrC, respectively.

2.3. Catalysts characterization

Catalysts characterizations were conducted by a series of technologies, not limited to scanning electron microscope (SEM), transmission electron microscope (TEM), X-ray photoelectron spectroscopy (XPS), electrochemical impedance spectroscopy (EIS), hydrogen temperature-programmed reduction (H_2-TPR) and oxygen temperature-programmed desorption (O_2-TPD). The details can be found in Text S2.

2.4. Catalytic experiments and analytical methods

The typical experiment of CIP degradation in batch-scale was performed under the following conditions: 25 ± 1 °C, 10 mg/L CIP, 0.1 g/L SSC and 1 mM PMS. Methanol (MeOH) and turt-butylalcohol (TBA) were selected as scavengers to identify $SO_4^{-\bullet}$ and HO•. Ultra-high-performance liquid chromatography-tandem mass spectrometry (UPLC-MS) was adopted to detect and analyze the intermediates of organics degradation. Electron paramagnetic resonance (EPR) was applied to monitor the generated reactive species and high-valent Co species during PMS activation. Cyclic tests were carried out to examine the reusability of SSC700. Detailed experimental procedures are available in Text S3.

Fix-bed continuous-flow tests with RhB as the target pollutant were conducted to evaluate the feasibility of SSC700 catalyst in packed state for industrial application. Experimental details are presented in Text S4.

Additionally, SSC700 membrane/PMS coupling systems were constructed to assess their capability and stability of mineralizing organics and resisting membrane fouling under long-lasting and high-flux operations. Fig. S1 illustrates the experimental setup for membrane tests. The investigations were carried out in both laboratory artificial wastewater and the secondary effluent from a domestic wastewater treatment plant in Chengdu Tianfu New Area in China. For laboratory artificial wastewater, RhB was selected as the model pollutant and added into deionized water. Regarding the secondary effluent, different concentrations of CIP, RhB and SMR were deliberately added into the effluent, respectively. The preparation method for membranes and the corresponding operating conditions in tests are described in Text S5.

EIS tests and current-time chronoamperometry measurements were performed to analyze the relationship between electrical conductivity and PMS activation. Text S6 presents the procedures in detail.

3. Results and discussion

3.1. Characterization of SSC catalysts

XRD analysis was performed to characterize the phase purity of the synthesized catalysts (Fig. 1a). Diffraction peaks of all the catalysts agreed well with the standard pattern of SSC (JCPDS card no. 00–053–0112). No prominent secondary peak was observed in all the patterns, indicating the successful preparation of SSC catalysts. High calcination temperature promoted the maturation and coarseness of grains, reflected by the increased peak intensity. Using the Scherrer equation based on the X-ray line broadening technique performed on the (110) diffraction peak, the equivalent crystallite sizes of SSC600, SSC700, SSC800 and SSC900 were determined to be 13.7, 18.8, 19.4 and 41.2 nm, respectively. The morphology of the typical catalyst SSC700 is shown in Fig. 1b. A peculiar three-dimensional (3D) network structure from glycine-assisted combustion synthesis was observed, which might benefit the mass transfer during organics decay. TEM photograph in Fig. 1c also reveals the abundance of micropores in the SSC700 catalyst. The particle size was about 20 nm, in accord with XRD calculation results. In the HRTEM diagram (Fig. 1d), the lattice spacing corresponding to the (110) crystal plane of SSC was measured to be 0.275 nm, matching well with the previous report [19]. Fig. S2a displays N_2 adsorption-desorption isotherms of the SSC700 catalyst at 77 K, and the BET SSA was determined to be 29.8 m^2/g. Fig. S2b shows that the majority of pores were smaller than 10 nm, which might serve as suitable channels for fast mass transport of both reactants and products.

3.2. Catalytic activity of SSC and the effects of coexisting ions and natural organics

Fig. 2a presents the influences of Sm/Sr ratio in the A-site of perovskite on the performances of catalysts for CIP degradation. Evidently, SrC was much more active than SmC, and higher content of Sr in the A-site favored PMS-mediated CIP oxidation. Intriguingly, SSC700 exhibited the highest activity, indicating an obvious synergy between Sm and Sr for PMS activation. This ravishing scenario has never been reported before, and elaborate investigations should be designed to decipher the underlying mechanisms in the near future.

Fig. 2b displays the performances of SSC catalysts in PMS activation for CIP degradation. Adsorption induced by SSC calcined at different temperatures made negligible contributions to CIP removal (no more than 10%), although the catalysts possessed abundant micropores and appreciable SSA. Given that ROS released by PMS self-oxidation may play roles in CIP oxidation, the performance of PMS alone was also examined in Fig. 2b. Obviously, about 23% of CIP was removed within 40 min by PMS alone. This is insignificant compared to the scenarios with the coexistence of SSC catalysts. To be precise, SSC700 attained complete removal of CIP after 40 min reaction, and the apparent reaction rate constant k_{app} reached 0.286 min^{-1}. A lower or higher calcination temperature during SSC preparation had adverse effects on PMS activation. This may be related to the physical-chemical properties of SSC catalysts, such as phase stability, chemical states of elements, electrical conductivity, and redox capability (discussed later).

In SSC700/PMS system, PMS concentration exerted significant effects on CIP removal (Fig. S3a). 0.5 mM PMS could not provide CIP with enough ROS to attain fast degradation, especially in the early stage. Compared with 1 mM PMS, the promoting effects of 2 mM PMS was limited, which may be ascribed to self-quenching of the proliferated ROS. Thus, 1 mM PMS was adopted in the following experiments. For SSC700/PMS, increasing temperature kinetically facilitates PMS activation and organics mineralization (Fig. S3b), and the reaction activation energy *Ea* was calculated to be 47.4 kJ/mol (the inset of Fig. S3b), comparable with previous results [20]. Initial pH had significant impacts on CIP oxidation by SSC700/PMS, and the degradation was inhibited in basic solution (Fig. S3c). The determined isoelectric point

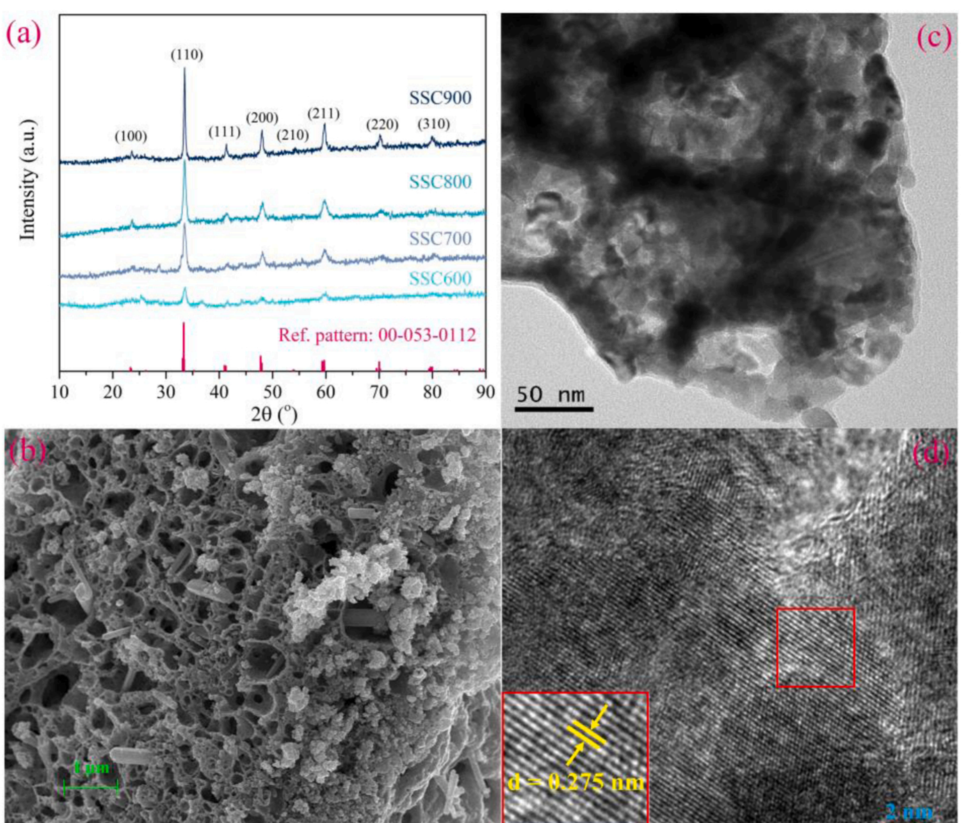

Fig. 1. (a) XRD patterns of SSC catalysts calcined at different temperatures; and (b) SEM, (c) TEM and (d) HRTEM images of SSC700.

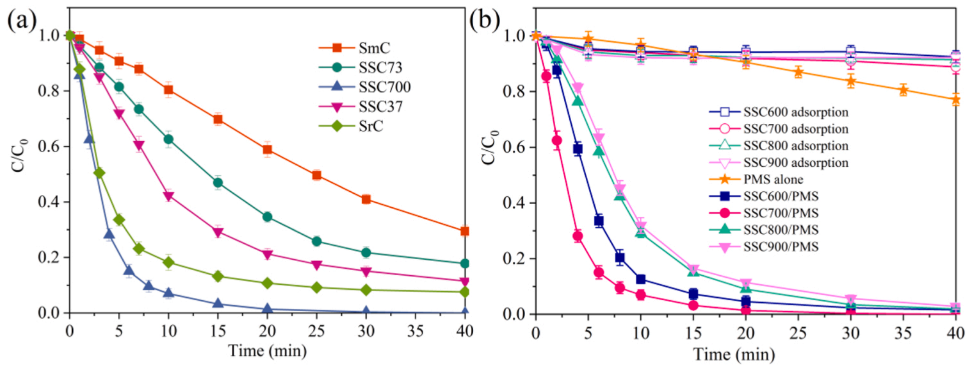

Fig. 2. CIP removal in different systems: the effects of (a) Sm/Sr ratio in catalyst and (b) calcination temperature of the catalyst (Experimental conditions: [catalyst] = 0.1 g/L, [CIP] = 10 mg/L, [PMS] = 1 mM, T = 25 °C and unadjusted pH).

(pH_{pzc}, 4.1) of SSC700 can theoretically account for the pH-dependent scenarios (Fig. S3d). Since the natural water body is generally at neutral or near-neutral pH, SSC700 is expected to exhibit prominent performance in PMS-mediated wastewater decontamination. The effects of the common inorganic anions and HA, a representative of natural organic matters (NOMs), on CIP decay were also examined (Fig. S4). Collectively, Cl^- and HCO_3^- played somewhat negative roles in organics degradation, while the others showed no visible influences on the process, indicative of superb adaptability of SSC700 for wastewater remediation. More details referring to the effects of reaction temperature, initial pH and the diverse water matrices are discussed in Text S7.

3.3. Stability and long-lasting performance of SSC700 membranes

To evaluate the stability of SSC700, cyclic experiments were conducted. Fig. 3a compares CIP removal efficiency in five runs. Briefly, SSC700 showed remarkable performance and high stability for PMS activation toward CIP decay. CIP attained 97.4% removal efficiency in the second run within 40 min, although k_{app} decreased to 0.184 min^{-1} (Fig. S5). In the following three runs, effective CIP degradation was still realized, and k_{app} was experimentally determined to be 0.160, 0.137 and 0.134 min^{-1}, respectively, indicating the high structural and surface stability of SSC700. Therefore, it is anticipated that SSC700 would demonstrate long-lasting performance in practical application.

Using RhB as a model pollutant, a fix-bed continuous-flow investigation was carried out to evaluate the feasibility of applying SSC700/PMS system on a pilot and potentially industrial scale. The apparent velocity of fluid flow was determined to be around 3.9 mm/min, and the mean retention time of liquid was calculated to be 2.6 min. As expected, in Fig. 3b, RhB can be continuously and completely degraded by SSC700/PMS for 12 h. Afterward, the removal efficiency of RhB slightly declined to about 90% at the 15th h. The decreased capacity may be attributed to adsorption-induced shielding of active sites. Active components loss caused by the long-term acidic shower may be another reason for efficacy decrease. In spite of this, SSC700 outperformed previously reported catalysts, e.g., nitrogen-doped carbon nanotubes/stainless steel fibers (N-CNTs/PSSF), which merely maintained high phenol removal efficiency for 2 h in a fixed-bed reactor due to surface oxidation of the carbonaceous catalysts [21]. Therefore, SSC700 has great potential for continuous-flow operations in fix-bed and liquid-solid reaction systems.

Membrane separation has been extensively applied in drinking water and wastewater treatment due to compactness, robustness, and high efficiency [22]. However, membrane fouling has been an intractable problem perplexing scientists worldwide, especially in the treatments of actual surface water and the secondary effluent, where native NOMs contribute the most to the serious irreversible membrane fouling [23]. Hence, we constructed innovative SSC700 membranes to evaluate their efficacy and stability under long-term high-flux operations for PMS activation and contaminants mineralization in DI water and the secondary effluent from a domestic wastewater treatment plant, respectively.

To obtain a stable SSC700 membrane, the effects of ultrasonic treatment (10, 20 and 30 min) for particle refinement and dispersion were evaluated first. Table S1 summarizes the pH_{pzc}, porosity and particle size distributions of the SSC700 membranes treated for different times. Generally, a long-time ultrasonic treatment resulted in lower pH_{pzc}, lower porosity and smaller particles, which would subsequently cause high fluid-flow resistance and poor permeability of membranes. As expected in Fig. S6a, the SSC700 membrane after ultrasonically

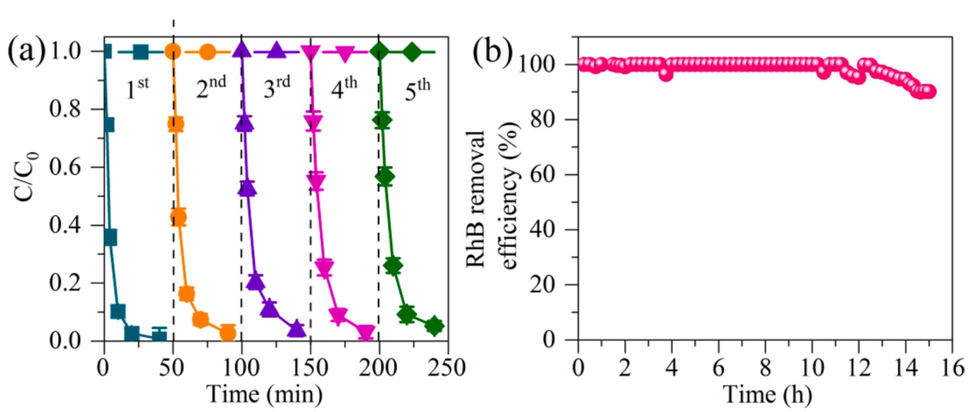

Fig. 3. (a) Reusability of SSC700 catalyst for CIP degradation in cycle tests (Experimental conditions: [SSC700] = 0.1 g/L, [CIP] = 10 mg/L, [PMS] = 1 mM, T = 25 °C and unadjusted pH); and (b) RhB degradation by SSC700/PMS system in a fixed-bed continuous reactor (Experimental conditions: [RhB] = 20 mg/L, [PMS] = 1 mM, T = 25 °C, unadjusted pH, and volume flow rate = 110 mL/min).

treated for 10 min demonstrated high activity for the complete removal of RhB within 24 h. The removal efficiency started to sharply decrease from the 25th h on, implying that a short-time ultrasonic treatment (10 min) cannot afford SSC700 membrane with long-lasting capability for highly-effective removal of pollutants due to the exorbitant flux. The short retention time determined by bigger particle-mediated higher porosity cannot constantly satisfy the prerequisite for thorough RhB degradation. On the other hand, particles with bigger size possess relatively fewer active sites for catalysis, and long-time soaking in acidic solution inevitably led some of them to flow away, thereby decreasing RhB removal efficiency. Partial occupation of active sites by organics adsorption might also account for the declined performance. On the contrary, just as the above statement, a long-time ultrasonic treatment (30 min, Fig. S6b) led to a compact membrane with low permeability, although RhB attained almost 100% removal within 30 h due to adequate retention time.

Fig. 4a presents the performance of the SSC700 membrane fabricated by 20-min ultrasonic treatment for 50-h continuous removal of RhB in DI water. To clearly explain its prominence, the variation of flux is also displayed. According to the diameter and thickness of SSC700 membrane, the mean apparent retention time (ART) was determined as well (Eq. (S2)). In the beginning, the flow rate reached 1.45 L/h (flux 1279.2 L/(m^2·h)) and RhB can be completely degraded with ART less than 3 s. Due to the increase of flow resistance caused by continuous vacuum filtration, the flow rate gradually decreased to about 0.475 L/h (flux 419.0 L/(m^2·h)) within 35 h. During this stage, RhB attained over 99% removal. Afterwards, the removal efficiency slowly decreased to 91.1% at the 50th h. In the whole process, the flow rate and ART were effectively kept over 0.42 L/h (flux over 368 L/(m^2·h)) and below 10 s, respectively, indicating the speedy generation of ROS for ultrafast RhB degradation. To evaluate the effects of ART on the mineralization degree of organics and the intermediates, TOC removal efficiencies at the 20th h in the three cases (The ART at the 20th h in the three membranes was 6, 7 and 10.2 s, respectively) were measured and are compared in Fig. S6c. Evidently, longer ART induced more TOC removal. In addition, ~40% RhB realized mineralization within 10 s, even though the real retention time was shorter than ART in view of membrane's porosity. Thus, under this operation mode, ROS can approach extremely high utilization efficiency, far surpassing batch-scale treatments. In a recent CoAl-layered double hydroxide nanosheet membrane (LDHm)/PMS system, when water flux was controlled at 80 L/(m^2·h) (lower than one-fourth of the lowest value in this work), the removal efficiency of ranitidine (2.5 mg/L) attained about 90% within 29 h [24]. Likewise, a Fe/activated carbon (Fe/AC) membrane fabricated by Chen et al. displayed great antifouling ability, and the dye molecules attained ~100% degradation within 11 h under a flux of over 165.0 L/(m^2·h) [25]. Apparently, SSC700 membrane here outperformed these membranes, with nearly complete removal of RhB for 35 h under fluxes over 419.0 L/(m^2·h). Fig. 4b shows the variation of Co leaching concentration during the 50-h operation. It basically presented a falling trend within the whole process and, more importantly, the effluent at any time satisfied the requirements of national standard for Co discharge (1 mg/L). To evaluate the contributions of the leaching Co ions during the process, RhB degradation by Co^{2+} with the corresponding concentration at each sampling point in Fig. 4b were carried out. In each test, the reaction time was determined by the corresponding mean ART in Fig. 4a. For example, at the 10th h, the leaching Co^{2+} and the mean ART were 0.084 mg/L and 5.6 s, respectively, and then RhB degradation was carried out for 5.6 s with 0.084 mg/L Co^{2+} as the initiator. In Fig. 4c, the leaching Co^{2+}-initiated PMS catalysis made negligible contributions to RhB removal, implying the decisive roles of SSC700 membrane. For membrane processes, the trifling contributions of the highly-active leaching Co^{2+} were primarily attributed to their low concentrations and the instantaneous retention. By contrast, the abundant Co species in SSC700 membranes provided substantial active sites for ROS generation, thereby promoting organics' rapid degradation. To assess the relationships between SSC700

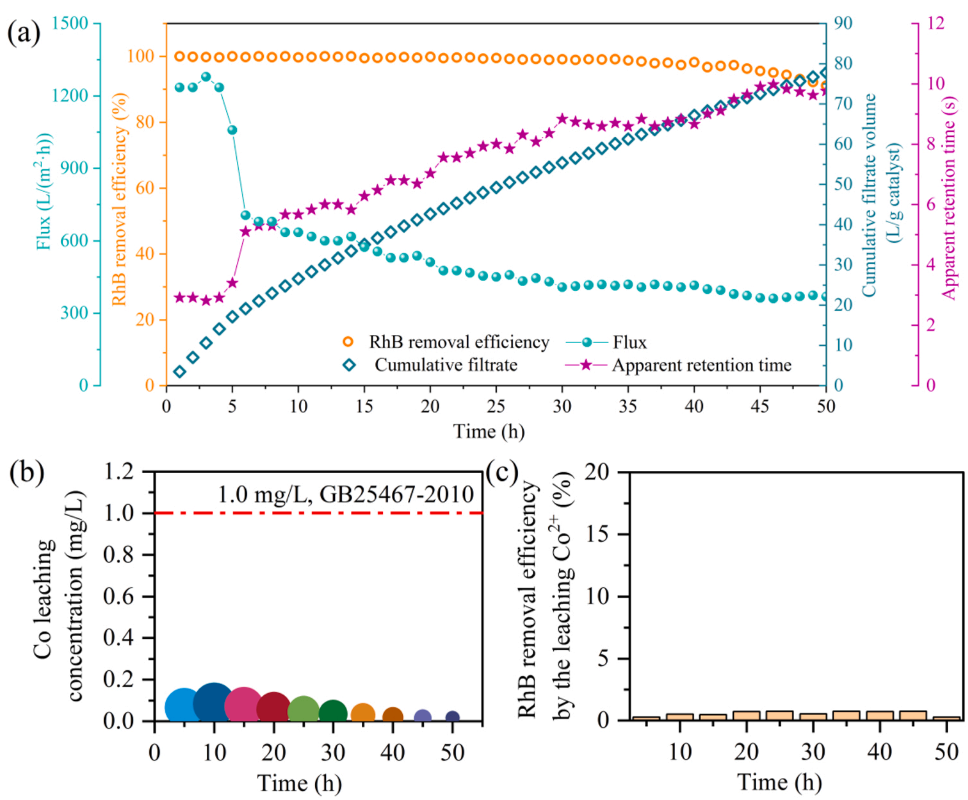

Fig. 4. (a) Long-lasting performance of SSC700 membrane on RhB degradation in DI water; and (b) Co leaching concentrations and (c) the contributions of the leaching Co ions during the 50-hour degradation of RhB by SSC700 membrane/PMS coupling system (Experimental conditions: Ultrasonic treatment time = 20 min, [RhB] = 20 mg/L, [PMS] = 1 mM, T = 25 °C, unadjusted pH, and operating vacuum degree = 0.09 MPa).

membrane's activity recession and the leaching Sm^{3+}/Sr^{2+}, their contributions to RhB oxidation were determined by the same way as the above. Fig. S7 displays the evolution of the leaching Sr^{2+}/Sm^{3+} concentrations during membrane operation. Agreeing with the results in Fig. 2a, both of them exhibited activity for PMS activation toward RhB decay. Still, the contributions by the leaching species were insignificant compared to the bulk. These irrefutable proofs confirm that PS-AOPs/membrane coupling technology is a feasible strategy for decontaminating wastewater.

The natural water differs greatly from artificial water in laboratory in the co-existence of diverse inorganic ions and NOMs, which generally cause the Achilles' heel of membrane separation technology. Thus, we evaluated the performance of SSC700 membrane/PMS system on the decay of CIP, RhB and SMR in the secondary effluent from a domestic wastewater treatment plant, respectively. The general water quality parameters of the secondary effluent were measured and are displayed in Table S2.

Fig. 5a shows the degradation of CIP in the secondary effluent by SSC700 membrane/PMS under 50-h operation, as well as the corresponding processing parameters. Collectively, SSC700 membrane exhibited a prominent stability from a hydraulic point of view, with flux leisurely decreasing from the original 1387.1–917.2 L/(m^2·h) under a constant transmembrane pressure of 0.09 MPa. Accordingly, ART gently crept from 5.2 to 7.9 s. Benefited from the high activity of SSC700 and the well-developed porous structure of membrane, CIP attained effective removal of over 60% in the whole process, confirming the high activity, long-term stability and eminent fouling resistance of SSC700 membrane. To further verify this, the concentration of the residual PMS at a time interval of 5 h was measured during CIP oxidation in the secondary effluent (Fig. S8). Although PMS consumption was less than 50% after the fluid flow penetrated SSC700 membrane, the residual PMS in the filtrate can be further decomposed by the leaching Co/Sm/Sr ions, thus facilitating the on-going mineralization of organics in the solution. Actually, membrane separation-PMS oxidation integrated systems were revealed to dramatically mitigate membrane fouling, and diverse catalysts loaded on ceramic membranes were reported to not only mineralize pollutants but also degrade NOMs, thus promoting resistance against surface and/or pore fouling by NOMs [26]. In a recent study, a $CuFe_2O_4$ tailored ceramic membrane exhibited prominent efficiency for HA removal, oxidizing them into conjugated structures of smaller molecular weight, and thereby inducing decreased irreversible fouling resistance [27]. Since the capability of Co species for the degradation of organics and NOMs was proved to be much higher than other common metal oxides [26,28], we prefer to emphasize the critical roles of Co species in SSC700 in the mineralization of contaminants and NOMs in the secondary effluent. This hypothesis can be solidly supported by the latest findings, where macromolecular and humic substances were effectively torn into small molecular organics by carbon nanofiber supported Co_3O_4/PMS [29]. Likewise, in this work, the small intermediates can be further mineralized by SSC700 membrane/PMS, if ART permits, just as the scenarios in Fig. S6c. For more direct proofs, Fig. 5b-d present the fluorescence excitation-emission matrix (EEM) spectra of the collected secondary effluent. Compared with the raw water (Fig. 5b), the intensity of fluorophores dramatically increased upon the addition of 5 mg/L CIP (Fig. 5c). After filtration/oxidation by SSC700 membrane, the signals of fluorophores in the filtrate turned out to be very weak (Fig. 5d), suggesting fast mineralization of the artificially-added pollutants and the native NOMs in the secondary effluent. Additionally, the shredded fragments of NOMs may also re-agglomerate to form bigger particles due to unsaturated bonds [27], thus intensifying the repulsive interactions between NOMs and SSC700 membrane and transforming irreversible cake fouling into a reversible one. Hence, profiting from the high activity of SSC700 membrane for in-situ generation of ROS from PMS, the simultaneous mineralization of organics and NOMs in secondary effluent technically attained, remarkably alleviating membrane fouling through pore blocking and/or cake formation, which endows SSC700 membrane/PMS coupling system with praiseworthy features in wastewater decontamination and membrane defouling.

RhB was also selected to be a model pollutant and added into the secondary effluent to examine the generality of SSC700 membranes for diverse contaminants. As illustrated in Fig. 6a, RhB attained exceedingly stable degradation at 32 °C (room temperature) within 100 h, and more

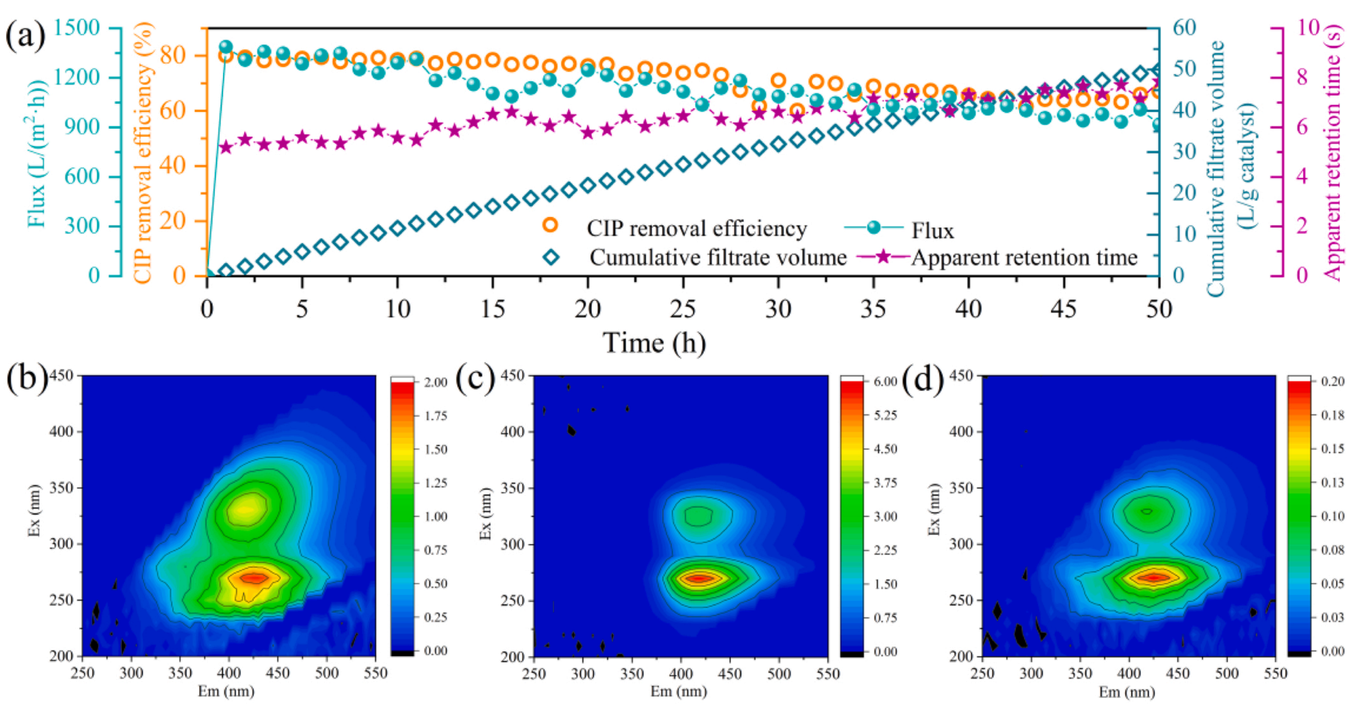

Fig. 5. (a) CIP degradation in the secondary effluent by SSC700 membrane/PMS (Experimental conditions: [CIP] = 5 mg/L, [PMS] = 1 mM, T = 25 °C, unadjusted pH, and operating vacuum degree = 0.09 MPa); and fluorescence EEM spectra of the secondary effluent: (b) raw water, (c) with the addition of CIP and (d) after treatment by SSC700 membrane/PMS.

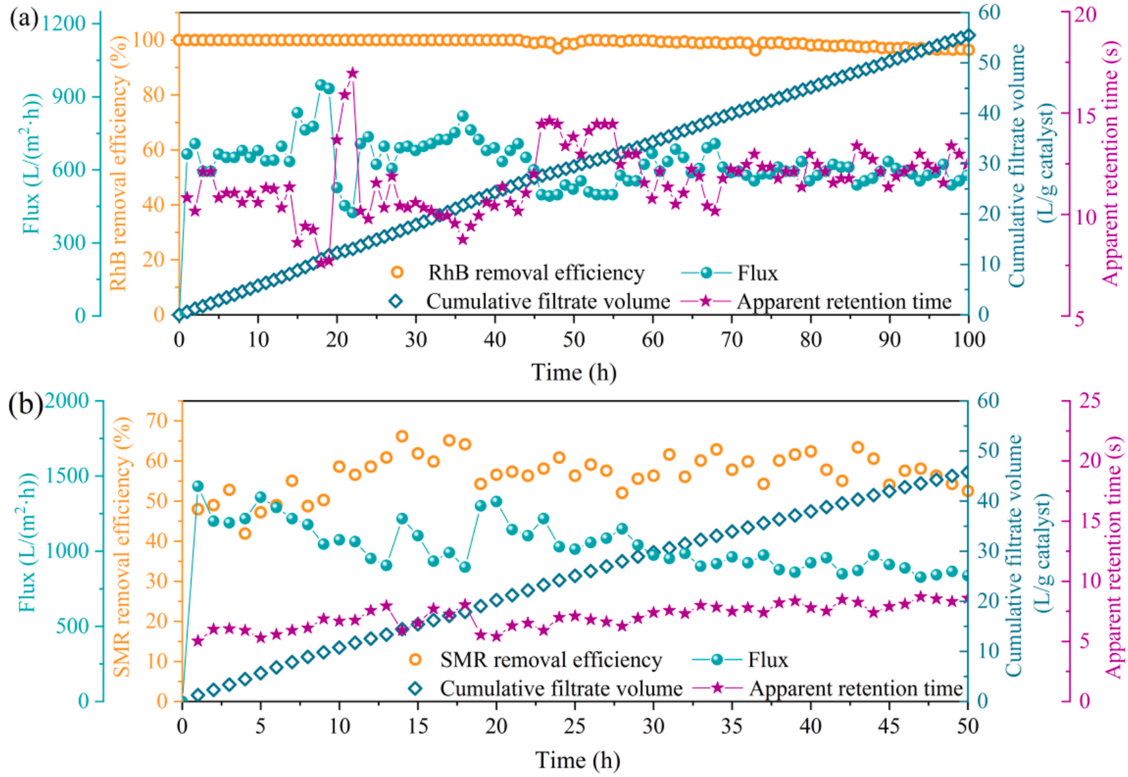

Fig. 6. Long-lasting performances of SSC700 membranes on organics degradation in the secondary effluent: (a) RhB (Experimental conditions: [RhB] = 20 mg/L, [PMS] = 1 mM, T = 32 °C, unadjusted pH, and operating vacuum degree = 0.09 MPa) and (b) SMR (Experimental conditions: [SMR] = 5 mg/L, [PMS] = 1 mM, T = 25 °C, unadjusted pH, and operating vacuum degree = 0.09 MPa).

than 95% of RhB could still be oxidized after 100-h reaction, suggesting marvelous activity and stability of SSC700 membrane in real wastewater. Moreover, during this long-term operation, the flux of filtrate remained around 600 L/(m^2·h) without obvious fall, indicative of remarkable hydraulic stability in application. In Fig. 6a, the ART of RhB molecules was less than 15 s, in which only a small amount of RhB can be removed in the batch-scale process (Fig. S9), confirming superb ROS utilization efficiency in membrane/PMS coupling system. According to the cumulative filtrate volume after 100-h running (55.5 L/g catalyst) and the dosage of SSC700 powder in batch processes (0.1 g/L), it can be inferred that SSC700 membrane/PMS separation-degradation strategy strikingly reduced the catalyst consumption by 82.0%, comparable to the level in a recent study [13]. Evidently, further increase of this index is confidently expected with a prolonged operation. These outcomes indicate that this unique route is greatly profitable for industrial practices due to the highly decreased investment in catalyst/oxidant.

We continued to select SMR (5 mg/L), a recalcitrant antibiotic, as another target pollutant to further assess the long-term efficacy of SSC700 membrane/PMS in real wastewater under high-flux operation. In Fig. 6b, with the flux ranging from 1400 to 800 L/(m^2·h) at 25 °C, about 50–60% of SMR can be effectively swept away with a short ART of 6–9 s. Thus, SMR removal flux can be estimated to be 2000 ~ 4200 mg/(m^2·h), two orders of magnitude higher than that of sulfamethoxazole (SMX) in a recent report, where only 22.15 mg/(m^2·h) was attained in carbonaceous composite membrane/PDS/tap water system within 24 h [30]. Note that the flux in SSC700 membrane/PMS/SMR system was higher than that of the RhB-involved system. This scenario is essentially attributed to the higher viscosity of RhB solution, leading to higher hydraulic resistance. From the membrane defouling point of view, SSC700 membranes fabricated here exerted magnificent performances in the three cases (CIP, RhB and SMR), because the filtrate fluxes did not exhibit extravagant variations during the long-term operations and only slight pulsations can be observed. This remarkable capacity of decomposing and/or tailoring organics/NOMs affords SSC700 membrane with prominent self-cleaning capability against fouling, making it a promising candidate for membrane/PS-AOPs coupling system in wastewater remediation.

3.4. *Possible catalytic reaction mechanisms*

To identify the ROS generated in SSC700/PMS system, quenching experiments were conducted using MeOH and TBA as scavengers, respectively. As described above, TBA could rapidly capture HO• due to the absence of α-H, whereas MeOH with α-H could readily react with both HO• and $SO_4^{-\bullet}$. As depicted in Fig. 7a, after adding 500 mM TBA, CIP degradation was moderately inhibited, and the removal efficiency decreased to 89.4% after a 40-min reaction. This demonstrates the participation of HO• in CIP degradation. Similarly, when 200 mM MeOH was added into the system, CIP degradation efficiency declined to 37.7%. Further rise of MeOH concentration resulted in more deleterious influences on CIP oxidation, and the removal efficiencies dropped to 24.6% and 17.7% in the presence of 500 mM and 2 M MeOH, respectively. The evidence implies the vital roles of $SO_4^{-\bullet}$ in CIP mineralization. Additionally, k_{app} was calculated and is displayed in Fig. 7b. Upon adding 0.5 M TBA, k_{app} decreased to 0.148 min^{-1}, whereas it was crippled to the degree below 10% in the presence of MeOH. These results indicate that HO• and $SO_4^{-\bullet}$ co-dominated the degradation of CIP. Nonetheless, visible removal of CIP can still be observed in Fig. 7a even with the presence of 2 M MeOH, indicating the possible participation of other ROS. Considering that the removal efficiency after 40-min reaction with 2 M MeOH was very close to the case without SSC in Fig. 2b, $^1O_2$ generated through self-oxidation of PMS had insignificant contribution to CIP oxidation, because 2 M MeOH can completely quench HO• and $SO_4^{-\bullet}$ generated by SSC700 catalysis [31].

Using DMPO and TEMP as spin-trapping agents for HO•/$SO_4^{-\bullet}$ and $^1O_2$, respectively, we carried out EPR measurements to further confirm

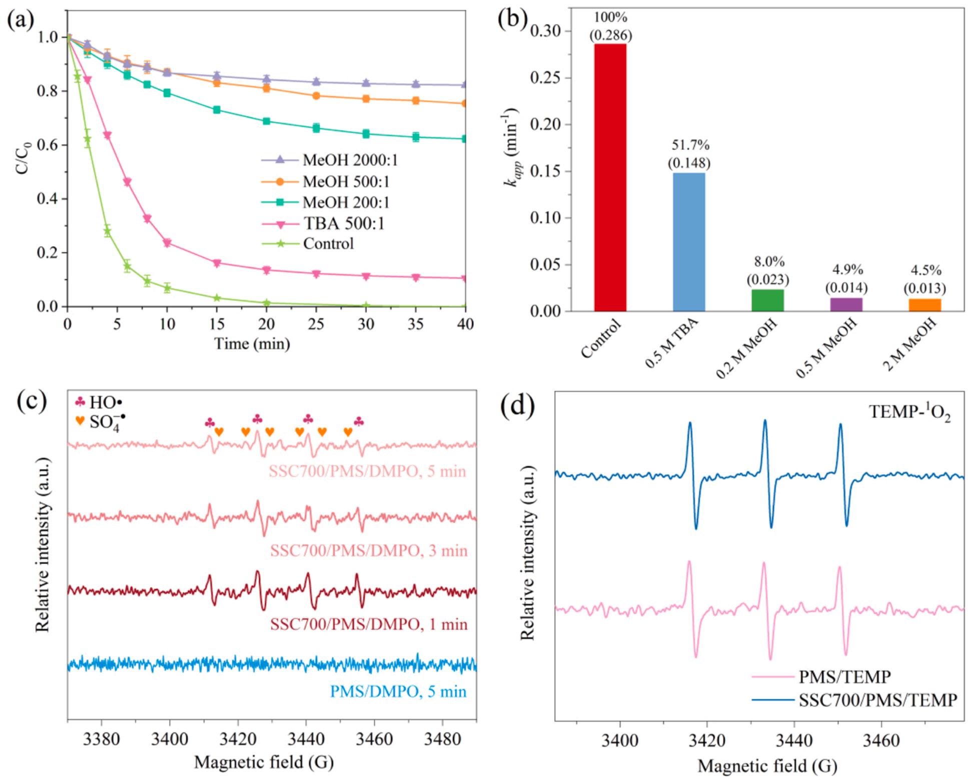

Fig. 7. (a) CIP degradation with the presence of TBA or MeOH (Experimental conditions: [SSC700] = 0.1 g/L, [CIP] = 10 mg/L, [PMS] = 1 mM, [TBA] = 500 mM, [MeOH] = 200–2000 mM, T = 25 °C and unadjusted pH); (b) k_{app} of CIP degradation in the systems listed in (a); and EPR spectra for (c) $SO_4^{\bullet -}$/HO• and (d) $^1O_2$ over SSC700/PMS system.

the responsible active species. As shown in Fig. 7c, without SSC700, the system did not show visible signals. Upon addition of SSC700, the signals of quartet lines with peaks strength of 1:2:2:1 were observed, attributed to DMPO-HO• adducts (the complex of DMPO and HO•). Meanwhile, the characteristic signals corresponding to the complex of DMPO and $SO_4^{\bullet -}$ were also discovered. Furthermore, the peak intensity decreased with the prolongation of reaction time, suggesting the quenching and/or extinction of HO•/ $SO_4^{\bullet -}$. These results verify that HO•/$SO_4^{\bullet -}$ were responsible for organics degradation, agreeing well with the above quenching experiments. To be precise, $O_2^{\bullet -}$ was also monitored by EPR tests, and the signals of DMPO-$O_2^{\bullet -}$ adduct in Fig. S10 verified the existence of $O_2^{\bullet -}$. Since the second-order rate constants of $O_2^{\bullet -}$ with alcohols are very low ($< 10^3$ M^{-1} s^{-1}) [32], the contribution of $O_2^{\bullet -}$ could not be covered by MeOH quenching if $O_2^{\bullet -}$ did participate in CIP degradation. Thus, it is reasonable to infer that $O_2^{\bullet -}$ played negligible roles in CIP oxidation. As for $^1O_2$, FFA was adopted as a chemical probe to identify the generation of $^1O_2$ due to their high rate constant of 1.2×10^8 M^{-1} s^{-1} [33]. However, FFA was also reported readily reacting with HO• ($k_{FFA,\bullet OH}$ 1.5×10^{10} M^{-1} s^{-1}) [33]. Hence, to exclude the interference of HO•, MeOH (2 M) was added to the SSC700/PMS/FFA system. As presented in Fig. S11, after a 40-min reaction, FFA attained no more than 15% removal efficiency, comparable to the adsorption by porous SSC700. However, MeOH can still react with $^1O_2$ ($k_{MeOH,^1O_2}$ 3.0×10^3 M^{-1} s^{-1}) [34]. The produced $^1O_2$ here might be partially quenched by the high-concentration MeOH, because the value of $k_{MeOH,^1O_2} \times [MeOH]$ (6.0×10^3 s^{-1}) was comparable with that of $k_{FFA,^1O_2} \times [FFA]$ (1.2×10^3 s^{-1}). Thus, to verify this speculation, EPR signals referring to 2,2,6,6-tetramethyl-1-piperidinyloxyl (TEMPO, the oxidation product of TEMP by $^1O_2$ or $O_2^{\bullet -}$) were detected in TEMP/PMS/SSC700 system (Fig. 7d). The signal intensity did not change visibly upon the addition of SSC700, proving the incapability of generating $^1O_2$ in SSC700/PMS. Therefore, consistent with the quenching results, HO• and $SO_4^{\bullet -}$ dominated organics oxidation.

To reveal the underlying mechanism of PMS activation over SSC, XPS analyses were performed before and after oxidation to profile the chemical composition and surface element bonding configuration of SSC700. As displayed in Fig. 8a, the XPS survey spectra of the both exhibited the existence of Sm, Sr, Co and O elements, although the signals related to Sm and Sr in the spectra of the spent SSC700 were feeble, which may be caused by the long-time acid etching (pH < 4, 50 h). Regarding perovskite catalysts, A-site elements are commonly inert to the catalytic reaction. However, in Fig. S7, Sm^{3+} and Sr^{2+} contributed to organics degradation. Furthermore, A-site elements significantly affected perovskite's activity (Fig. 2a). Thus, the activity recession of SSC700 membrane may, to some extent, relate to the loss of Sm/Sr. B-site transition metals are generally considered as the active sites in perovskites. For Co 2p in the fresh SSC700 (Fig. 8b), further deconvolution indicated that the two peaks at 779.7 (Co $2p_{3/2}$) and 794.8 eV (Co $2p_{1/2}$) could be ascribed to Co^{3+}, while the peaks at 780.8 (Co $2p_{3/2}$) and 796.2 eV (Co $2p_{1/2}$) could be assigned to Co^{2+} [35]. Additionally, the peak at 789.8 eV was linked to the satellite peak of Co 2p. After 50-hour PMS activation, the spectrum of Co 2p could be deconvoluted into three components. Except for the peaks corresponding to Co^{3+} (779.3 and 794.3 eV) and Co^{2+} (780.3 and 795.3 eV), respectively, the new peaks located at 781.4 and 796.6 eV can be ascribed to Co^{4+} [36], suggesting that some low-valent Co species were oxidized to Co^{4+} during PMS activation. To confirm the formation of Co^{4+}, EPR measurements were carried out to monitor the variation of Co species in SSC700 during PMS activation. In Fig. S12, the resonances with g ~ 4.343 could be ascribed to Co^{2+} species, and the signals appearing upon the addition of PMS could be assigned to Co^{4+} (g ~ 4.708 and g ~ 2.170) [37], indicating the generation of Co^{4+} during SSC700-induced PMS activation. This is entirely consistent with XPS results. Table 1 summarizes the relative contents of each element in different valence states before and after oxidation. The relative content

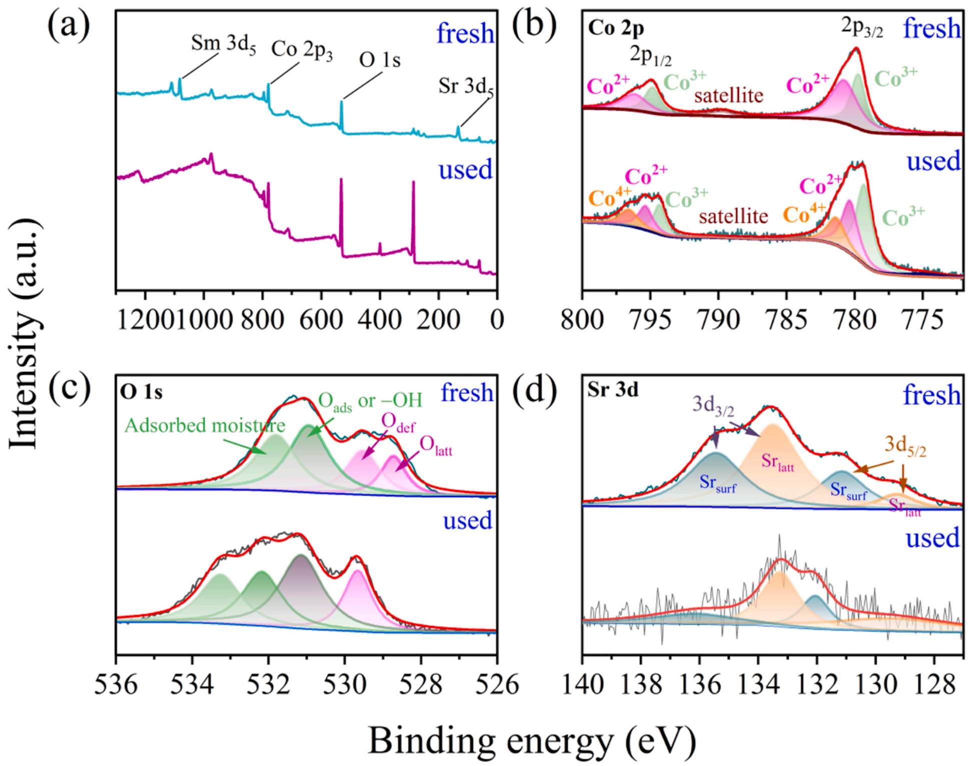

Fig. 8. XPS spectra of (a) wide survey, (b) Co 2p, (c) O 1 s and (d) Sr 3d of the fresh and used SSC700.

Table 1
XPS fitting results of the key elements in different chemical states in the fresh and used SSC700.

Sample	Co			O				Sr	
	Co^{2+}	Co^{3+}	Co^{4+}	O_{latt}	O_{def}	O_{ads}/−OH	H_2O	Sr_{latt}	Sr_{surf}
Fresh SSC700	780.8 eV, 796.2 eV 56.1%	779.7 eV, 794.8 eV 43.9%	—	528.7 eV 13.3%	529.5 eV 19.7%	530.9 eV 36.0%	531.8 eV 31%	129.3 eV, 133.5 eV 51.4%	131.2 eV, 135.4 eV 48.6%
Spent SSC700	780.3 eV, 795.3 eV 32.3%	779.3 eV, 794.3 eV 44.9%	781.4 eV, 796.6 eV 22.8%	529.7 eV 19.2%	531.1 eV 35.0%	532.2 eV 23.4%	533.3 eV 22.4%	129.5 eV, 133.3 eV 66.2%	132.1 eV, 136.1 eV 33.8%

of Co^{3+} did not change significantly, whereas that of Co^{2+} greatly decreased from 56.1% to 32.3%, indicating the crucial role of low-valent Co^{2+} in PMS activation. Generally, low-valent Co species are much more active in decomposing PMS than their high-valent counterparts due to their stronger redox capability. Recently, we constructed the valence states–catalysis relationships; low-valent Co species overshadowed the others in terms of ROS generation [35]. Therefore, Co^{2+} might be responsible for PMS activation and the subsequent organics oxidation in this work.

Surface oxygen species were revealed to efficiently improve the catalytic activity of perovskites [38]. Hence, it is essential to analyze the variations of surface oxygen species before and after PMS activation. In the case of O 1 s (Fig. 8c), the spectrum of fresh SSC700 can be fitted into four subpeaks located at 528.7, 529.5, 530.9 and 531.8 eV, corresponding to lattice oxygen species (O^{2-}, O_{latt}), highly oxidative oxygen species (O_2^{2-}/O^-, O_{def}), surface-adsorbed oxygen species or hydroxyl groups (O_{ads} or −OH), and the surface-adsorbed water (H_2O), respectively [39]. For the spent SSC700, all four subpeaks shifted to higher binding energies, and they can still be orderly assigned to the above four oxygen species [40]. Specifically, the relative contents of O_{def} and O_{ads}/−OH experienced substantial changes: the relative content of O_{ads}/−OH decreased by 12.6%, while that of O_{def} increased by 15.3% (Table 1). These results suggest that surface oxygen species might play essential roles in PMS chemistry. Similar increased O_{def} was reported recently, i.e., relatively weakly-bound surface oxygen species produced by the labile O_{latt} could be converted to active oxygen (O_{def}), which subsequently transformed into ROS with the presence of PMS [38]. In this work, instead of O_{latt}, O_{ads}/−OH were responsible for the enrichment of O_{def} and facilitated ROS production. Additionally, the loss of the surface enriched Sr and Sm (see Fig. 8a and S7) might be another reason for O_{def} increase (the detailed analysis is available in Text S8). Furthermore, Duan et al. revealed that when a water molecule was adjacent to a persulfate molecule on the surface of a carbocatalyst, the significantly lengthened H−O bond in H_2O tended to donate electrons to the carbon matrix, facilitating the cleavage of the prolonged O−O bond in PS and the production of HO• [41]. The water molecules at a spatial advantage can be oxidized by PS. Given the higher activity of surface −OH and the asymmetry of PMS, we hypothesize that surface adsorbed –OH is also inclined to donate electrons to SSC700 to transform O_{ads} into O_{def}. Simultaneously, PMS was activated upon interaction with SSC700. These processes promoted the generation of HO• and $SO_4^{-\bullet}$, accounting for the above-stated long-lasting performance of the high-flux SSC700 membrane.

To confirm the catalytic roles of B-site Co active sites and oxygen species in redox reactions, H_2-TPR and O_2-TPD tests for catalysts calcined at different temperatures were carried out. The H_2-TPR profile

of Co-containing perovskites can be divided into four stages, i.e., stage I (100–360 °C, reduction of O_{ads} and O_{def}), stage II (360–390 °C, Co^{3+} to Co^{2+}), stage III (450–600 °C, surface Co^{2+} to Co^0), and stage IV (> 600 °C, bulk Co^{2+} to metallic Co) [12,42,43]. Generally, lower reduction temperature corresponds to better redox capability. Compared to SSC600, SSC800 and SSC900, both O_{ads}/O_{def} and surface Co^{2+} of SSC700 were more vulnerable to being reduced, reflected by the lowest reduction temperature in each stage (Fig. 9a) (more details are available in Text S9). Thus, it is reasonable for SSC700 to present the highest activity for ROS generation. The O_2-TPD profiles in Fig. 9b further prove the merits of SSC700 in terms of the amount of surface adsorbed oxygen species. With the increase of operating temperature, the weakly bound adsorbed oxygen species (< 250 °C), surface lattice oxygen (250 –530 °C) and bulk lattice oxygen (> 530 °C) sequentially desorbed [43]. Evidently, SSC700 possessed the most abundant surface adsorbed oxygen species, which have been labeled as active sites for PMS decomposition and ROS generation in XPS analysis (see deep discussions in Text S10). Therefore, in combination with the stronger capability for electron transfer (Fig. 9c and d, discussed in Text S11), the abundant surface adsorbed oxygen species and the reactive surface $Co^{2+}/Co^{3+}/Co^{4+}$ redox couple jointly accounted for the high activity of SSC700 toward PMS activation and contaminants mineralization.

Based on the above findings, low-valent Co^{2+} may preferentially react with PMS to produce HO• and $SO_4^{-\bullet}$, with itself being oxidized into Co^{3+} or Co^{4+} (Eqs. (1)–(4)). Co^{3+} was also likely to be oxidized to Co^{4+} by PMS (Eqs. (5) and (6)). Inversely, high-valent Co^{4+} could be reduced by HSO_5^- to produce Co^{3+} and subsequently, Co^{2+} (Eqs. (7) and (8)). Co^{4+} species with a negative charge-transfer energy value ($\Delta < -2$ eV) promoted the electrical conductivity of catalysts, and demonstrated a high capacity to withdraw electrons and activate peroxide O–O bond [44]. Therefore, the produced Co^{4+} active sites in SSC700 in turn facilitated the $Co^{4+}/Co^{3+}/Co^{2+}$ redox cycle for radical generation. Of note, the comproportionation reaction between Co^{4+} and Co^{2+} might occur as well (Eq. (9)). On the whole, as illustrated in Fig. 10, in combination with the surface adsorbed oxygen species (O_{ads} or –OH), these

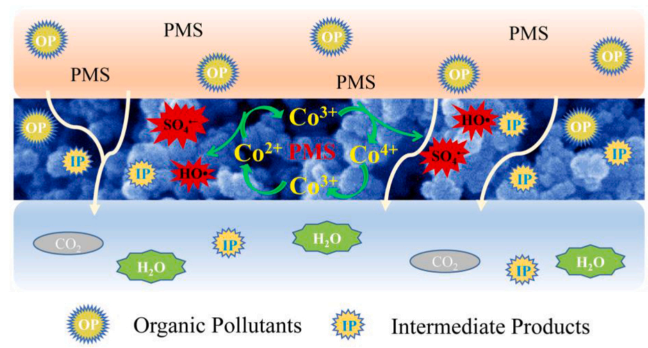

Fig. 10. Possible mechanisms for the generation of reactive species in the SSC700 membrane/PMS coupling system.

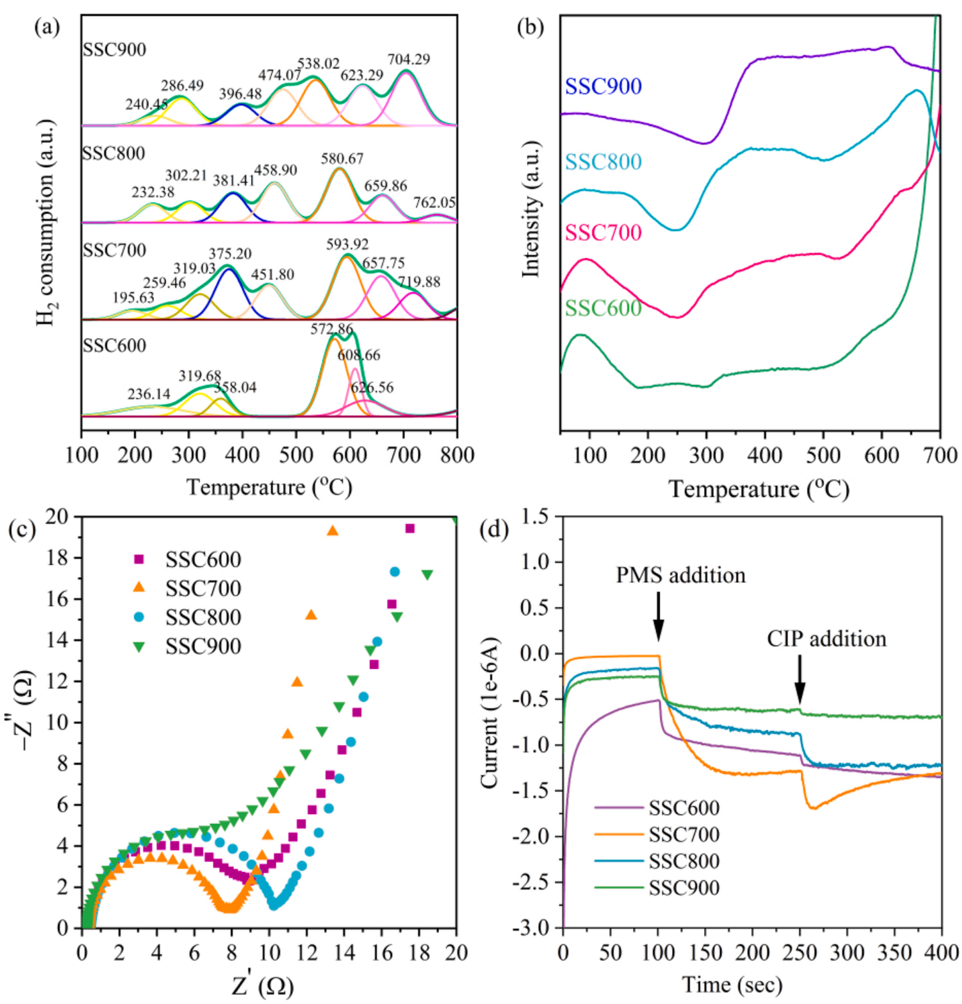

Fig. 9. (a) H_2-TPR, (b) O_2-TPD and (c) Nyquist profiles of SSC600, SSC700, SSC800 and SSC900 catalysts; and (d) Current-time curves of SSC600/PMS, SSC700/PMS, SSC800/PMS and SSC900/PMS systems.

redox-active components ensured the continuous generation of HO• and $SO_4^{-\bullet}$, thereby accelerating the effective degradation of pollutants during long-lasting high-flux membrane filtration. Noticeably, although the knowledge about Sm/Sr-induced PMS activation remains ambiguous, their contributions to ROS generation from PMS cannot be excluded.

$$Co^{2+} + 2HSO_5^- \rightarrow Co^{4+} + 2SO_4^{2-} + 2HO^\bullet \tag{1}$$

$$Co^{2+} + 2HSO_5^- \rightarrow Co^{4+} + 2SO_4^{-\bullet} + 2OH^- \tag{2}$$

$$Co^{2+} + HSO_5^- \rightarrow Co^{3+} + SO_4^{2-} + HO^\bullet \tag{3}$$

$$Co^{2+} + HSO_5^- \rightarrow Co^{3+} + SO_4^{-\bullet} + OH^- \tag{4}$$

$$Co^{3+} + HSO_5^- \rightarrow Co^{4+} + SO_4^{2-} + HO^\bullet \tag{5}$$

$$Co^{3+} + HSO_5^- \rightarrow Co^{4+} + SO_4^{-\bullet} + OH^- \tag{6}$$

$$Co^{4+} + HSO_5^- \rightarrow Co^{3+} + SO_5^{-\bullet} + H^+ \tag{7}$$

$$Co^{3+} + HSO_5^- \rightarrow Co^{2+} + SO_5^{-\bullet} + H^+ \tag{8}$$

$$Co^{2+} + Co^{4+} \rightarrow 2Co^{3+} \tag{9}$$

3.5. Proposed CIP degradation pathways and predicted toxicity

UPLC-MS analyzed the possible intermediates of CIP degradation and the results are presented in Figs. S13–S19 (The possible pathways of RhB/SMR degradation were also discussed and are available in Text S12). According to the detected seven intermediates, three possible CIP degradation pathways were proposed. As displayed in Fig. 11, pathway I could be defined as a defluorination process [45]. After the defluorination reaction, the oxidation of piperazine ring happened, forming P1 (*m/z* 301). Subsequently, under the attack of ROS, P1 was oxidized through quinolone ring oxidation and the cleavage of the derivative of the piperazine ring, producing P2 (*m/z* 129) and other fragments. Pathway II was quinolone ring oxidation, similar to a previous study [46]. Under the attack of HO•/$SO_4^{-\bullet}$, the oxidation of quinolone ring first happened, producing P3 (*m/z* 340). A series of ring-opening and defluorination processes further led to P4 (*m/z* 133). Pathway III generally referred to the oxidation of the piperazine ring. The produced intermediate P5 (*m/z* 318) subsequently went through quinolone ring oxidation and gradually transformed to P6 (*m/z* 129) and P7 (*m/z* 120). Ultimately, the intermediates mentioned above and the fragments in each pathway in Fig. 11 could be further degraded into H_2O, CO_2 and other smaller products.

We evaluated the toxicity of the intermediates (P1-P7) based on "ecological structure-activity relationships" using the ECOSAR program [47]. As shown in Fig. 12, CIP, P1, P2, P3, P4 and P5 are acutely and chronically not harmful to fish, daphnia and green algae, while P6 and P7 show toxicity toward these organisms. Specifically, P6 is acutely toxic for fish and daphnia and very toxic for green algae. From a chronic point of view, it is also toxic for all of them. From Fig. 11, P6 has the same *m/z* as P2 and P2 probably was the dominant form of the intermediates with *m/z* 129 due to its reasonable downstream fragments. Thus, we speculate that the amount of P6 in the effluents of the CIP/SSC700/PMS system was insignificant. Chronically speaking, P7 is harmful to fish and green algae and toxic for daphnia. These outcomes imply that the evolution of effluent toxicity cannot be neglected. Deep mineralization by perovskite-induced radical oxidation for a longer processing time will address the issues.

4. Conclusions

To conclude, a perovskite catalyst $Sm_{0.5}Sr_{0.5}CoO_{3-\delta}$ (SSC700) was prepared through glycine-assisted solution combustion and calcination. The excellent catalytic performance of SSC700 for PMS activation toward organics degradation resulted from its reactive surface Co^{2+}, abundant surface adsorbed oxygen species, and high capability for electron transfer. HO• and $SO_4^{-\bullet}$ were responsible for contaminants mineralization. SSC700 demonstrated superb adaptability for diverse inorganic ions and NOMs except for HCO_3^-. More importantly, SSC700

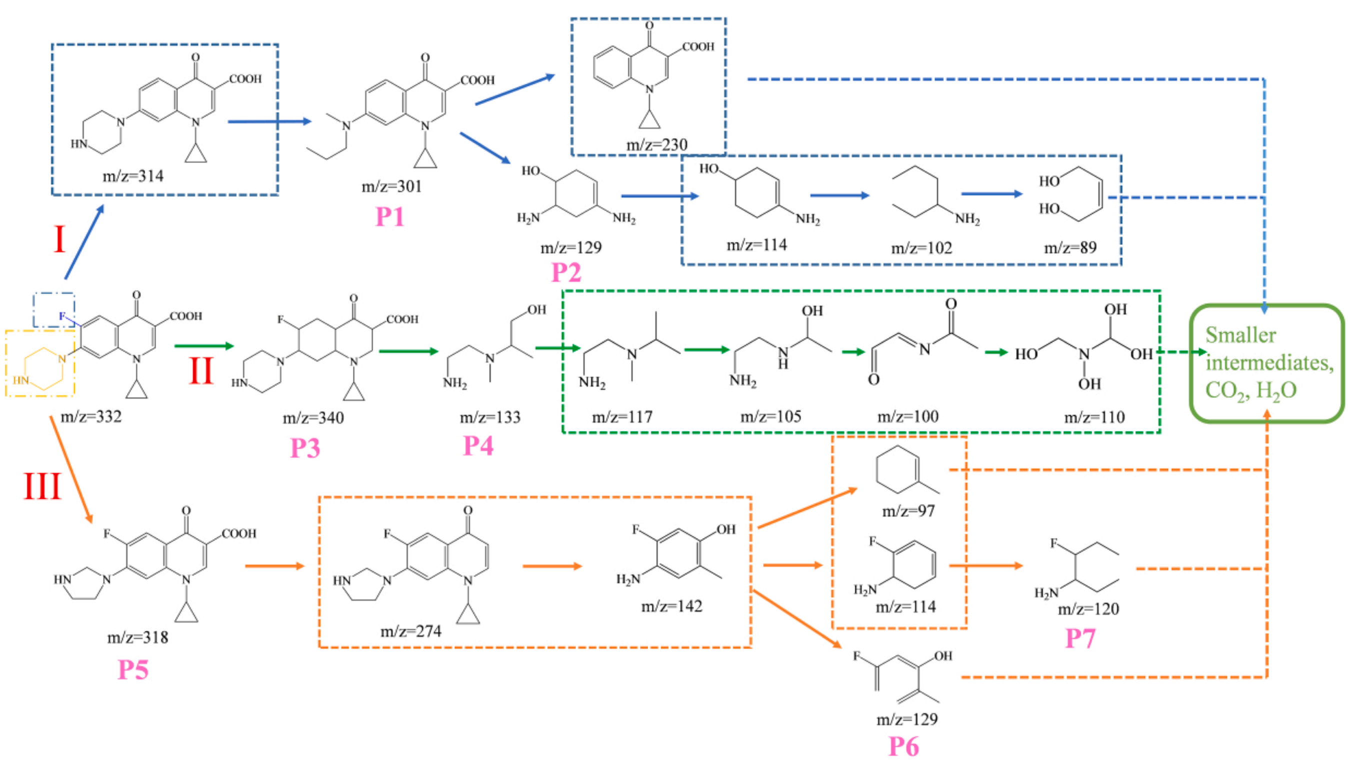

Fig. 11. Proposed CIP degradation pathways in SSC700/PMS system.

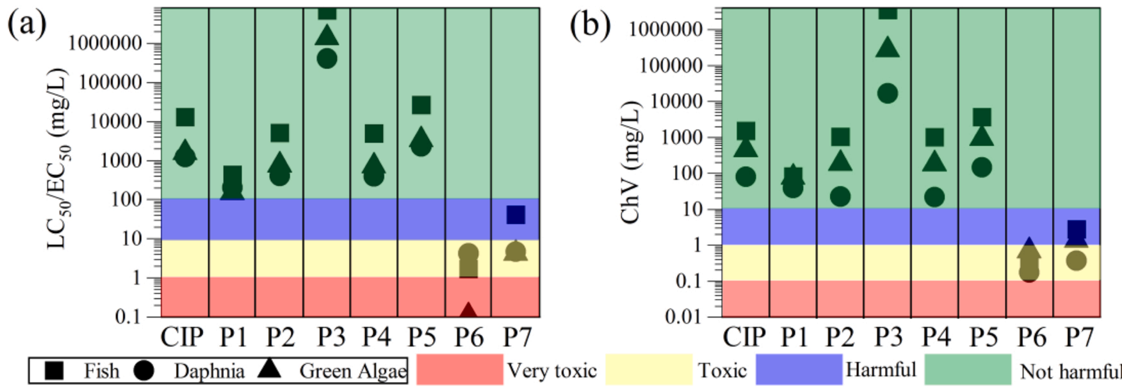

Fig. 12. (a) Acute and (b) chronic toxicity of the intermediates during CIP degradation process by SSC700/PMS.

exhibited prominent stability, without apparent performance recession in multicycle tests. In fix-bed continuous flow experiments, pollutants achieved fast removal in the SSC700/PMS system, attaining 100% removal efficiency within 12 h and maintaining it above 90% in 15 h.

Additionally, with the backgrounds of both model wastewater and the secondary effluent, the constructed SSC700 membrane/PMS coupling systems displayed marvelous long-lasting performances for in-situ generation of ROS under high-flux operations, demonstrating striking capability for wastewater remediation and membrane defouling against NOMs. The highly reactive $Co^{2+}/Co^{3+}/Co^{4+}$ redox loop and the abundant surface adsorbed oxygen species collaboratively accounted for the superior activity and stability for radical generation in long-term operations. On the basis of UPLC-MS analysis, three possible CIP degradation pathways were proposed, including defluorination, quinolone ring opening and piperazine ring oxidation. The toxicity assessment revealed the toxicity of some intermediates, and the issue could be overcome by deeper radical mineralization with prolonged treatment. This study preliminarily unveils the potential of SSC700 membrane/PMS as a far-reaching strategy for wastewater decontamination and membrane defouling. Further work referring to the meticulous design and fabrication of concrete perovskite ceramic membranes with high activity, superb stability and good fluid permeability may accelerate the application in practice.

CRediT authorship contribution statement

Jinping Liang: Conceptualization, Methodology, Investigation, Writing – original draft, Funding acquisition. **Kai Gao**: Investigation. **Aijuan Zhou**: Investigation. **Yuqiao Fang**: Investigation. **Shengyou Su**: Investigation. **Ling Fu**: Investigation. **Mingchao Sun**: Discussion. **Xiaoguang Duan**: Discussion, Writing – review & editing, Supervision.

Declaration of Competing Interest

The authors declare that they have no known competing financial interests or personal relationships that could have appeared to influence the work reported in this paper.

Data availability

Data will be made available on request.

Acknowledgments

We gratefully thank Prof. Dr. Wanglai Cen in Sichuan University for H_2-TPR and O_2-TPD tests. The research was supported by Sichuan Engineering Laboratory of Livestock Manure Treatment and Recycling (China) (202103).

Appendix A. Supporting information

Supplementary data associated with this article can be found in the online version at doi:10.1016/j.apcatb.2023.122440.

References

[1] J. Lee, U. von Gunten, J.-H. Kim, Persulfate-based advanced oxidation: critical assessment of opportunities and roadblocks, Environ. Sci. Technol. 54 (2020) 3064–3081, https://doi.org/10.1021/acs.est.9b07082.

[2] Y. Gong, X. Zhao, H. Zhang, B. Yang, K. Xiao, T. Guo, J. Zhang, H. Shao, Y. Wang, G. Yu, MOF-derived nitrogen doped carbon modified g-C_3N_4 heterostructure composite with enhanced photocatalytic activity for bisphenol A degradation with peroxymonosulfate under visible light irradiation, Appl. Catal. B Environ. 233 (2018) 35–45, https://doi.org/10.1016/j.apcatb.2018.03.077.

[3] X. Duan, C. Su, J. Miao, Y. Zhong, Z. Shao, S. Wang, H. Sun, Insights into perovskite-catalyzed peroxymonosulfate activation: maneuverable cobalt sites for promoted evolution of sulfate radicals, Appl. Catal. B Environ. 220 (2018) 626–634, https://doi.org/10.1016/j.apcatb.2017.08.088.

[4] H. Milh, D. Cabooter, R. Dewil, Role of process parameters in the degradation of sulfamethoxazole by heat-activated peroxymonosulfate oxidation: radical identification and elucidation of the degradation mechanism, Chem. Eng. J. 422 (2021), 130457, https://doi.org/10.1016/j.cej.2021.130457.

[5] Y. Gao, T. Wu, C. Yang, C. Ma, Z. Zhao, Z. Wu, S. Cao, W. Geng, Y. Wang, Y. Yao, Y. Zhang, C. Cheng, Activity trends and mechanisms in peroxymonosulfate-assisted catalytic production of singlet oxygen over atomic metal-N-C catalysts, Angew. Chem. Int. Ed. 60 (2021) 22513–22521, https://doi.org/10.1002/anie.202109530.

[6] Y.-J. Zhang, G.-X. Huang, L.R. Winter, J.-J. Chen, L. Tian, S.-C. Mei, Z. Zhang, F. Chen, Z.-Y. Guo, R. Ji, Y.-Z. You, W.-W. Li, X.-W. Liu, H.-Q. Yu, M. Elimelech, Simultaneous nanocatalytic surface activation of pollutants and oxidants for highly efficient water decontamination, Nat. Commun. 13 (2022) 3005, https://doi.org/10.1038/s41467-022-30560-9.

[7] Q. Yang, Y. Chen, X. Duan, S. Zhou, Y. Niu, H. Sun, L. Zhi, S. Wang, Unzipping carbon nanotubes to nanoribbons for revealing the mechanism of nonradical oxidation by carbocatalysis, Appl. Catal. B Environ. 276 (2020), 119146, https://doi.org/10.1016/j.apcatb.2020.119146.

[8] X. Duan, H. Sun, Z. Ao, L. Zhou, G. Wang, S. Wang, Unveiling the active sites of graphene-catalyzed peroxymonosulfate activation, Carbon 107 (2016) 371–378, https://doi.org/10.1016/j.carbon.2016.06.016.

[9] J. Miao, X.G. Duan, J. Li, J. Dai, B. Liu, S.B. Wang, W. Zhou, Z.P. Shao, Boosting performance of lanthanide magnetism perovskite for advanced oxidation through lattice doping with catalytically inert element, Chem. Eng. J. 355 (2019) 721–730, https://doi.org/10.1016/j.cej.2018.08.192.

[10] J. Qi, X. Yang, P.-Y. Pan, T. Huang, X. Yang, C.-C. Wang, W. Liu, Interface engineering of $Co(OH)_2$ nanosheets growing on the $KNbO_3$ perovskite based on electronic structure modulation for enhanced peroxymonosulfate activation, Environ. Sci. Technol. 56 (2022) 5200–5212, https://doi.org/10.1021/acs.est.1c08806.

[11] Q. Pan, Q. Gao, G. Gao, M. Liu, B. Han, K. Xia, C. Zhou, Composition-engineered $LaCoO_3$-based monolithic catalysts for easily operational and robust peroxymonosulfate activation, Chem. Eng. J. 424 (2021), 130574, https://doi.org/10.1016/j.cej.2021.130574.

[12] P. Liang, D.D. Meng, Y. Liang, Z. Wang, C. Zhang, S.B. Wang, Z.H. Zhang, Cation deficiency tuned $LaCoO_{3-\delta}$ perovskite for peroxymonosulfate activation towards bisphenol A degradation, Chem. Eng. J. 409 (2021), 128196, https://doi.org/10.1016/j.cej.2020.128196.

[13] Z. Qiu, X. Xiao, W. Yu, X. Zhu, C. Chu, B. Chen, Selective separation catalysis membrane for highly efficient water and soil decontamination via a persulfate-based advanced oxidation process, Environ. Sci. Technol. 56 (2022) 3234–3244, https://doi.org/10.1021/acs.est.1c06721.

[14] Y. Dong, H. Wu, F. Yang, S. Gray, Cost and efficiency perspectives of ceramic membranes for water treatment, Water Res. 220 (2022), 118629, https://doi.org/10.1016/j.watres.2022.118629.

[15] Y. Liu, Q. Lin, Y. Guo, J. Zhao, X. Luo, H. Zhang, G. Li, H. Liang, The nitrogen-doped multi-walled carbon nanotubes modified membrane activated peroxymonosulfate for enhanced degradation of organics and membrane fouling mitigation in natural waters treatment, Water Res. 209 (2022), 117960, https://doi.org/10.1016/j.watres.2021.117960.

[16] Y. Bao, W.J. Lee, T.-T. Lim, R. Wang, X. Hu, Pore-functionalized ceramic membrane with isotropically impregnated cobalt oxide for sulfamethoxazole degradation and membrane fouling elimination: synergistic effect between catalytic oxidation and membrane separation, Appl. Catal. B Environ. 254 (2019) 37–46, https://doi.org/10.1016/j.apcatb.2019.04.081.

[17] S. Wang, J. Tian, Q. Wang, Z. Zhao, F. Cui, G. Li, Low-temperature sintered high-strength CuO doped ceramic hollow fiber membrane: preparation, characterization and catalytic activity, J. Membr. Sci. 570–571 (2019) 333–342, https://doi.org/10.1016/j.memsci.2018.10.078.

[18] M. Zhu, J. Miao, D.Q. Guan, Y.J. Zhong, R. Ran, S.B. Wang, W. Zhou, Z.P. Shao, Efficient wastewater remediation enabled by self-assembled perovskite oxide heterostructures with multiple reaction pathways, ACS Sustain. Chem. Eng. 8 (2020) 6033–6042, https://doi.org/10.1021/acssuschemeng.0c00882.

[19] J. Jing, M.N. Pervez, P. Sun, C. Cao, B. Li, V. Naddeo, W. Jin, Y. Zhao, Highly efficient removal of bisphenol A by a novel Co-doped $LaFeO_3$ perovskite/PMS system in salinity water, Sci. Total Environ. 801 (2021), 149490, https://doi.org/10.1016/j.scitotenv.2021.149490.

[20] J. Liang, L. Fu, Activation of peroxymonosulfate (PMS) by Co_3O_4 quantum dots decorated hierarchical C@Co_3O_4 for degradation of organic pollutants: kinetics and radical-nonradical cooperation mechanisms, Appl. Surf. Sci. 563 (2021), 150335, https://doi.org/10.1016/j.apsusc.2021.150335.

[21] X. Tian, H. Huang, H. Zhang, Y. Yan, Preparation of structured N-CNTs/PSSF composite catalyst to activate peroxymonosulfate for phenol degradation, Sep. Purif. Technol. 290 (2022), 120903, https://doi.org/10.1016/j.seppur.2022.120903.

[22] M.B. Asif, Z. Zhang, Ceramic membrane technology for water and wastewater treatment: a critical review of performance, full-scale applications, membrane fouling and prospects, Chem. Eng. J. 418 (2021), 129481, https://doi.org/10.1016/j.cej.2021.129481.

[23] J. Adusei-Gyamfi, B. Ouddane, L. Rietveld, J.-P. Cornard, J. Criquet, Natural organic matter-cations complexation and its impact on water treatment: a critical review, Water Res. 160 (2019) 130–147, https://doi.org/10.1016/j.watres.2019.05.064.

[24] M.B. Asif, H. Kang, Z. Zhang, Gravity-driven layered double hydroxide nanosheet membrane activated peroxymonosulfate system for micropollutant degradation, J. Hazard. Mater. 425 (2022), 127988, https://doi.org/10.1016/j.jhazmat.2021.127988.

[25] L. Chen, X. Ren, Y. Li, D. Hu, X. Feng, Y. Liu, J. Zhao, High flux Fe/activated carbon membranes for efficient degradation of organic pollutants in water by activating sodium persulfate, Sep. Purif. Technol. 285 (2022), 120411, https://doi.org/10.1016/j.seppur.2021.120411.

[26] X. Cheng, P. Li, W. Liu, C. Luo, D. Wu, W. Zhou, L. Zheng, X. Zhu, H. Liang, Activation of peroxymonosulfate by metal oxide nanoparticles for mitigating organic membrane fouling in surface water treatment, Sep. Purif. Technol. 246 (2020), 116935, https://doi.org/10.1016/j.seppur.2020.116935.

[27] Y. Zhao, D. Lu, C. Xu, J. Zhong, M. Chen, S. Xu, Y. Cao, Q. Zhao, M. Yang, J. Ma, Synergistic oxidation - filtration process analysis of catalytic $CuFe_2O_4$ - tailored ceramic membrane filtration via peroxymonosulfate activation for humic acid treatment, Water Res. 171 (2020), 115387, https://doi.org/10.1016/j.watres.2019.115387.

[28] Z. Bai, S. Gao, H. Yu, X. Liu, J. Tian, Layered metal oxides loaded ceramic membrane activating peroxymonosulfate for mitigation of NOM membrane fouling, Water Res. 222 (2022), 118928, https://doi.org/10.1016/j.watres.2022.118928.

[29] Q. Fan, X. Cheng, X. Zhu, C. Luo, H. Ren, D. Wu, H. Liang, Secondary wastewater treatment using peroxymonosulfate activated by a carbon nanofiber supported Co_3O_4 (Co_3O_4@CNF) catalyst combined with ultrafiltration, Sep. Purif. Technol. 287 (2022), 120579, https://doi.org/10.1016/j.seppur.2022.120579.

[30] F. Qian, J. Luo, H. Yin, F. Liu, S. Gao, X. Gu, Carbonaceous composite membranes for peroxydisulfate activation to remove sulfamethoxazole in a real water matrix, Chemosphere 288 (2022), 132597, https://doi.org/10.1016/j.chemosphere.2021.132597.

[31] L. Wang, B. Li, D.D. Dionysiou, B. Chen, J. Yang, J. Li, Overlooked formation of H_2O_2 during the hydroxyl radical-scavenging process when using alcohols as scavengers, Environ. Sci. Technol. 56 (2022) 3386–3396, https://doi.org/10.1021/acs.est.1c03796.

[32] J.-C.E. Yang, Y. Lin, H.-H. Peng, B. Yuan, D.D. Dionysiou, X.-D. Huang, D.-D. Zhang, M.-L. Fu, Novel magnetic rod-like Mn-Fe oxycarbide toward peroxymonosulfate activation for efficient oxidation of butyl paraben: radical oxidation versus singlet oxygenation, Appl. Catal. B Environ. 268 (2020), 118549, https://doi.org/10.1016/j.apcatb.2019.118549.

[33] C. Zhu, Y. Zhang, Z. Fan, F. Liu, A. Li, Carbonate-enhanced catalytic activity and stability of Co_3O_4 nanowires for $^1O_2$-driven bisphenol A degradation via peroxymonosulfate activation: critical roles of electron and proton acceptors, J. Hazard. Mater. 393 (2020), 122395, https://doi.org/10.1016/j.jhazmat.2020.122395.

[34] W. Ren, C. Cheng, P. Shao, X. Luo, H. Zhang, S. Wang, X. Duan, Origins of electron-transfer regime in persulfate-based nonradical oxidation processes, Environ. Sci. Technol. 56 (2022) 78–97, https://doi.org/10.1021/acs.est.1c05374.

[35] J. Liang, L. Fu, K. Gao, X. Duan, Accelerating radical generation from peroxymonosulfate by confined variable Co species toward ciprofloxacin mineralization: ROS quantification and mechanisms elucidation, Appl. Catal. B Environ. 315 (2022), 121542, https://doi.org/10.1016/j.apcatb.2022.121542.

[36] Y. Niu, C. Sun, X. Song, X. Yin, N. Zhang, Porous structured $BaCo_{0.8}Nb_{0.1}Sc_{0.1}O_{3-\delta}$ perovskite synthesized by template method as high performance cathode for intermediate-temperature solid oxide fuel cells, J. Alloy. Compd. 828 (2020), 154291, https://doi.org/10.1016/j.jallcom.2020.154291.

[37] N. Yao, G. Wang, H. Jia, J. Yin, H. Cong, S. Chen, W. Luo, Intermolecular energy gap-induced formation of high-valent cobalt species in CoOOH surface layer on cobalt sulfides for efficient water oxidation, Angew. Chem. Int. Ed. 61 (2022), e202117178, https://doi.org/10.1002/anie.202117178.

[38] H. Chen, Y. Xu, K. Zhu, H. Zhang, Understanding oxygen-deficient $La_2CuO_{4-\delta}$ perovskite activated peroxymonosulfate for bisphenol A degradation: the role of localized electron within oxygen vacancy, Appl. Catal. B Environ. 284 (2021), 119732, https://doi.org/10.1016/j.apcatb.2020.119732.

[39] J. Sun, L. Du, B. Sun, G. Han, Y. Ma, J. Wang, H. Huo, C. Du, G. Yin, Bifunctional $LaMn_{0.3}Co_{0.7}O_3$ perovskite oxide catalyst for oxygen reduction and evolution reactions: the optimized eg electronic structures by manganese dopant, ACS Appl. Mater. Interfaces 12 (2020) 24717–24725, https://doi.org/10.1021/acsami.0c03983.

[40] K. Sugahara, K. Kamata, S. Muratsugu, M. Hara, Amino acid-aided synthesis of a hexagonal $SrMnO_3$ nanoperovskite catalyst for aerobic oxidation, ACS Omega 2 (2017) 1608–1616, https://doi.org/10.1021/acsomega.7b00146.

[41] X.G. Duan, C. Su, L. Zhou, H.Q. Sun, A. Suvorova, T. Odedairo, Z.H. Zhu, Z.P. Shao, S.B. Wang, Surface controlled generation of reactive radicals from persulfate by carbocatalysis on nanodiamonds, Appl. Catal. B Environ. 194 (2016) 7–15, https://doi.org/10.1016/j.apcatb.2016.04.043.

[42] F. Fang, P. Zhao, N. Feng, H. Wan, G. Guan, Surface engineering on porous perovskite-type $La_{0.6}Sr_{0.4}CoO_{3-\delta}$ nanotubes for an enhanced performance in diesel soot elimination, J. Hazard. Mater. 399 (2020), 123014, https://doi.org/10.1016/j.jhazmat.2020.123014.

[43] J. Yang, S. Hu, L. Shi, S. Hoang, W. Yang, Y. Fang, Z. Liang, C. Pan, Y. Zhu, L. Li, J. Wu, J. Hu, Y. Guo, Oxygen vacancies and Lewis acid sites synergistically promoted catalytic methane combustion over perovskite oxides, Environ. Sci. Technol. 55 (2021) 9243–9254, https://doi.org/10.1021/acs.est.1c00511.

[44] M. Zhu, D. Guan, Z. Hu, H.-J. Lin, C.-T. Chen, H.-S. Sheu, S. Wang, J. Zhou, W. Zhou, Z. Shao, Synergistic effects in ordered Co oxides for boosting catalytic activity in advanced oxidation processes, Appl. Catal. B Environ. 297 (2021), 120463, https://doi.org/10.1016/j.apcatb.2021.120463.

[45] C. Liu, S. Mao, M. Shi, F. Wang, M. Xia, Q. Chen, X. Ju, Peroxymonosulfate activation through 2D/2D Z-scheme CoAl-LDH/BiOBr photocatalyst under visible light for ciprofloxacin degradation, J. Hazard. Mater. 420 (2021), 126613, https://doi.org/10.1016/j.jhazmat.2021.126613.

[46] G. Li, S. Zhou, Z. Shi, X. Meng, L. Li, B. Liu, Electrochemical degradation of ciprofloxacin on BDD anode using a differential column batch reactor: mechanisms, kinetics and pathways, Environ. Sci. Pollut. Res. 26 (2019) 17740–17750, https://doi.org/10.1007/s11356-019-04900-0.

[47] G. Li, X. Nie, Y. Gao, T. An, Can environmental pharmaceuticals be photocatalytically degraded and completely mineralized in water using g-C_3N_4/TiO_2 under visible light irradiation?—Implications of persistent toxic intermediates, Appl. Catal. B Environ. 180 (2016) 726–732, https://doi.org/10.1016/j.apcatb.2015.07.014.